

# Evaluation of an Urban Canopy Parameterization in a Mesoscale Model

Hung-Neng S. Chin, Martin J. Leach, Gayle A. Sugiyama, John M. Leone, Jr., Hoyt Walker, J.S. Nasstrom, Michael J. Brown

April 5, 2004

Monthly Weather Review

#### **Disclaimer**

This document was prepared as an account of work sponsored by an agency of the United States Government. Neither the United States Government nor the University of California nor any of their employees, makes any warranty, express or implied, or assumes any legal liability or responsibility for the accuracy, completeness, or usefulness of any information, apparatus, product, or process disclosed, or represents that its use would not infringe privately owned rights. Reference herein to any specific commercial product, process, or service by trade name, trademark, manufacturer, or otherwise, does not necessarily constitute or imply its endorsement, recommendation, or favoring by the United States Government or the University of California. The views and opinions of authors expressed herein do not necessarily state or reflect those of the United States Government or the University of California, and shall not be used for advertising or product endorsement purposes.

## Evaluation of an Urban Canopy Parameterization in a Mesoscale Model Using VTMX and URBAN 2000 Data

By

Hung-Neng S. Chin, Martin J. Leach, Gayle A. Sugiyama John M. Leone Jr., Hoyt Walker, and J. S. Nasstrom

> Atmospheric Science Division Lawrence Livermore National Laboratory Livermore, California

> > and

Michael J. Brown

Los Alamos National Laboratory Los Alamos, New Mexico

Submitted to the Monthly Weather Review (April, 2004)

Revised (October, 2004; January, 2005)

Accepted (January, 2005)

Corresponding author address: Dr. Chin, Lawrence Livermore National Laboratory, P. O. Box 808 (L-103), Livermore, CA 94551, Email: chin2@llnl.gov.

#### **Abstract**

A modified urban canopy parameterization (UCP) is developed and evaluated in a three-dimensional mesoscale model to assess the urban impact on surface and lower atmospheric properties. This parameterization accounts for the effects of building drag, turbulent production, radiation balance, anthropogenic heating, and building rooftop heating/cooling. USGS land-use data are also utilized to derive urban infrastructure and urban surface properties needed for driving the UCP. An intensive observational period with clear-sky, strong ambient wind and drainage flow, and the absence of land-lake breeze over the Salt Lake Valley, occurring on 25-26 October 2000, is selected for this study.

A series of sensitivity experiments are performed to gain understanding of the urban impact in the mesoscale model. Results indicate that within the selected urban environment, urban surface characteristics and anthropogenic heating play little role in the formation of the modeled nocturnal urban boundary layer. The rooftop effect appears to be the main contributor to this urban boundary layer. Sensitivity experiments also show that for this weak urban heat island case, the model horizontal grid resolution is important in simulating the elevated inversion layer.

The root mean square errors of the predicted wind and temperature with respect to surface station measurements exhibit substantially larger discrepancies at the urban locations than the rural counterparts. However, the close agreement of modeled tracer concentration with observations fairly justifies the modeled urban impact on the wind direction shift and wind drag effects.

## 1. Introduction

Urban infrastructure properties, such as building area size, building height, and street canyon impact the surface and atmospheric properties. The well-recognized urban heat island (UHI) phenomenon, characterized by a temperature contrast between the city and the surrounding rural area is one such impact, which can affect urban airflow, atmospheric dispersion and pollution behavior. This phenomenon typically coincides with the existence of a weakly unstable or neutral surface layer underneath an elevated inversion layer. The base of this inversion layer is used to define the urban boundary layer. Many field experiments documented this phenomenon, which typically occurs under clear skies with weak ambient wind conditions at night (Summers 1965; Bornstein 1968; Clarke 1969; Ching et al. 1978; Shreffler 1978; Uno et al. 1988), and may even be the cool island in the day (Garstang 1975; Oke 1982; Bornstein 1987).

The maximum magnitude of UHI effect varies from case to case, and is modulated by the prevailing synoptic weather conditions, especially cloud cover and wind speed. This magnitude can range from a few degrees to 12 °C (Oke 1973 and 1982). Weaker UHIs are usually seen in cloudy conditions as a result of reduced radiation fluxes in the urban-rural surface energy budgets. Earlier studies also found that the magnitude of UHI effect is inversely related to the wind speed due to the enhanced urban turbulence energy in reducing the urban-rural temperature contrast as the wind speed increases (Hildebrand and Ackerman 1984; Morris and Simmonds 2001). In addition, wind direction shifts of 10-20° by the urban impact have been detected in earlier field studies (Angell et al. 1971; Draxler 1986). Failure to incorporate this urban wind shift effect into numerical models could lead to significant error in plume trajectory calculations. Oke (1995) presents a comprehensive review of earlier observational studies on the characteristics, causes and effects of the urban heat island.

With the rapid growth of the world population, urbanization appears to be an important issue on environmental and health aspects. Almost two-thirds of the U.S. population lives in urbanized areas

occupying less than 2% of the land surface (Carbone 2000). Similar statistics of urbanization exist in other parts of the world. As a result, the interaction between an urban region and atmospheric processes becomes a very complicated problem. Therefore, further understanding of the urban impact via the surface-atmosphere interaction is important to improve weather forecasts, and to minimize losses caused by the weather-related events, and even by the terrorist threat.

Both the urban building infrastructure and underlying urban surface impact the evolution of the UHI and the heat island circulation. Most previous studies on the genesis of UHI have focused on the influence from the urban surface (Oke 1995). This includes the effects of urban surface characteristics and anthropogenic heating. Oke (1995) also pointed out that anthropogenic heating alone is unlikely to be a major contributor to the UHI in most cities. In contrast, the impact from the urban building infrastructure has been addressed less often in previous studies.

To consider the urban infrastructure effect in mesoscale models, a parameterization is required to account for the sub-grid building impacts on momentum and heat transfer, turbulence kinetic energy production, and surface energy budget. To this end, Brown and Williams (1998, hereafter referred to as BW) recently developed an urban canopy parameterization (UCP) to represent the urban infrastructure effect.

The addition of rooftop surface energy equation into the BW scheme can lead to a more reasonable diurnal cycle of the heat island effect (Chin et al. 2000). The details of this rooftop effect are described in Section 3a. In addition to the urban infrastructure effect, urban surface characteristics affect the surface momentum and heat budgets, and therefore indirectly impact the atmospheric transport and mixing processes.

Limited data prescribing the characteristics of the urban infrastructure and urban surface at different geographic locations present a major challenge for using an UCP in the mesoscale model. Our approach to this challenge is to use USGS land-use data to derive the required input parameters for the urban canopy scheme (Chin et al. 2002).

To verify the urban impact in the mesoscale model, the traditional approach of using single station data seems to be inadequate. There is a considerable bias on the sampling accuracy of the urban environment, particularly in strong wind conditions (Draxler 1986). The bias is due to buildings, other urban structures, and surfaces substantially perturbing the wind field and creating observations that are dominated by local circulation and thus inadequately representing the prevailing transport vector. Therefore, additional alternative of high spatial resolution data, such as tracer measurements become valuable for this purpose.

Three objectives are addressed in this study. The first objective is to evaluate the modified BW urban canopy scheme with the observed measurements. The second objective is to quantitatively gauge the relative contribution of urban infrastructure and urban surface to the overall urban effect on the mesoscale processes. Finally, the sensitivity of model grid horizontal resolution and urban morphology to the UCP is also explored.

This paper is presented in the following sections. Section 2 describes the model and its initialization, the experiment design of simulations, and instruments and observations used to validate the urban canopy scheme. The details of the UCP and its required input parameters are included in section 3. Results of the macroscopic aspects of urban impacts on the surface and low-level atmosphere, sensitivity of model grid resolution and urban morphology to the UCP, and the model validation with conventional station measurements and tracer concentration samplers are shown in section 4. A summary and discussion follow in section 5.

#### 2. MODEL DESCRIPTION, MEASUREMENTS AND EXPERIMENT DESIGN

## a. Model and Initial Conditions

A modified Naval Research Laboratory's (NRL's) three-dimensional Coupled ocean / Atmosphere Mesoscale Prediction System (COAMPS) is used to study the urban impacts on surface and lower atmospheric properties (Chin et al. 2000 and 2001). COAMPS consists of a data assimilation system, a nonhydrostatic atmospheric forecast model, and a hydrostatic ocean model.

In this study, we use only the atmospheric model. The reader is referred to Hodur (1997) for further details of COAMPS.

COAMPS can use a complete atmospheric data assimilation system, composed of data quality control, analysis, and initialization for real-data simulations. However, to minimize the impact of the data assimilation on the performance of UCP, the simulations are conducted without the data assimilation update cycle. In this study, the large-scale model data are used to provide the first guess to the analysis fields. These analysis fields are directly used as the initial conditions for the model simulations without using the multivariate optimum interpolation scheme to blend in observational data.

The model domain contains 35 grid points in the vertical, with the grid size varied to maximize resolution at lower levels. The grid spacing of the lowest layer is 4 m, with each successive layer aloft smoothly increased. Therefore, the model has very high vertical grid resolution near the ground to compute the building rooftop effect at every grid level. Totally, it contains 9 grid points below the altitude of 143 m with the corresponding grid spacing of 4, 4, 4, 6, 10, 14, 24, 42 and 70 m, respectively. The domain top resides at the altitude of 35.898 km.

In the horizontal, both coordinates have 61 grid points for all nest grid domains. A uniform grid size of 36 km is used for the outer coarse mesh. A constant grid size ratio of three is applied to define the inner nest grids. Up to a total of four nests are used in this study. Therefore, the grid resolutions for the inner nest grids are 12 km, 4 km, and 1.333 km, respectively.

Constant time steps of 90 and 45 seconds for non-sound and sound wave calculations, respectively, are adopted in the outer coarse grids for the time-splitting scheme. The time steps for the inner nest domains are reduced proportionally to the nest-grid size ratio. The rigid boundary condition is imposed at the vertical boundaries. A sponge-damping layer is placed above 12.8 km to minimize the reflection of internal gravity waves off the rigid upper boundary. The Davies (1976) boundary condition is applied to the lateral boundaries with a nudging zone of seven grid

points at each lateral boundary. A constant concentration of carbon dioxide at 300 ppm and climatological ozone profile from NRL's NOGAPS (Navy Operational Global Atmospheric Prediction System) data are used for radiation transfer calculation.

The initial and lateral boundary conditions of simulations are based on the ETA data with a horizontal resolution of 40 km from the National Centers for Environmental Prediction. The intensive observational period (IOP) occurring on 25-26 October during VTMX 2000 (IOP-10) is selected for this study as representative of high wind environment. The synoptic condition at 12Z 25 October 2000 indicated that a high-pressure center is located at about 250 km to the southeast of the Salt Lake Valley. Therefore, the prevailing southeasterly exists in the area of concern throughout the simulation course.

Typically, the UHI is defined by the temperature difference at 2 meters above the ground between the urban and rural sites. However, the heights of the temperature sensors at the available measurement sites were not generally 2 meters. During the IOP-10, a nighttime temperature difference of 2 °C was observed at two meso-net rural and urban stations (QSA and QHW), where the sensors were placed at 12 m. Another example of the temperature contrast by 3 °C at 6 m was observed between other stations (e.g., BB / QB at downtown, and rural station BLUF). An earlier observational study demonstrated that the maximum warming in an urban heat island occurs near the surface and decreases to the top of the urban canopy (Oke 1995). Therefore, this IOP falls into the lower end of the UHI spectrum as shown by Oke (1973, 1982). This result is consistent with the inverse correlation of UHI with the wind speed as reported by other investigators (Hildebrand and Ackerman 1984; Morris and Simmonds 2001).

The nighttime UHIs for another five IOPs with tracer releases (e.g., 2, 4, 5, 7, and 9) between station QSA and QHW are also computed and their maximum magnitudes ranges from 2 °C to 3 °C, which still falls into the weak UHI category. Therefore, the UHIs exhibit little difference among

these IOPs. However, the choice of IOP-10 for this study is owing to its stronger wind, which allows the UCP to detect the urban wind shift effect more easily on the tracer plume calculation.

In order to address the limitations inherent in individual station measurements, the concentration observations from the SF6 releases are also adopted to validate the urban impact in the mesoscale model. The wind field predictions along with stability indices from COAMPS simulations are used in the Lagrangian particle dispersion model (Ermak and Nasstrom 2000) to compute tracer concentrations. The observed hourly-integrated tracer surface concentrations are interpolated onto a 9 km x 9 km grid domain. The interpolation of measured tracer concentration is done using a nearest neighbor method (Akima 1978).

## b. Experiment Design

All simulations shown in this study start at 12Z 25 October 2000, and last for 36 hours of simulation time. A series of sensitivity experiments are conducted in this research. First, the sensitivity of initial roof temperature and roof properties (albedo and emissivity) is used to explore its impact on the model prediction. Second, simulations with and without the urban effect are performed to gauge the urban influence on the mesoscale processes. Third, simulations with the derived urban parameters from different resolutions of USGS land-use data (200 and 30 meters, respectively) and urban morphology are used to evaluate the sensitivity of urban parameters to the modeled urban effect. Finally, the experiments with different levels of nest grids (i.e., 3 and 4 nests) are conducted to study the impact of horizontal resolution on the UCP. For all simulations shown with the urban impact, the UCP is turned on only in the most inner grid domain.

## c. Instruments and Observations

The Department of Energy sponsored two concurrent field campaigns in October 2000. The Vertical Transport and Mixing Experiment (VTMX), funded by the Experimental Meteorology Program, was designed to study vertical mixing in the Salt Lake City (SLC) Basin due to the mesoscale processes that occur in the mountain-valley region. The Chemical and Biological

National Security Program (CBNP) supported additional meteorological instruments and tracer sampling capabilities within the urban core of SLC. The domain coverage and available instruments of VTMX 2000 and URBAN 2000 can been seen in Figure 2 of Allwine et al. (2002).

Due to the limited availability of the vertical profiles of measurements, particularly the temperature field in the areas with the simulated urban boundary layer, the model verification of this study is mainly focused on the near-surface fields. The data from surface stations in the Utah meso-net located within the urban domain were visually checked for excessive wind-speed spiking or wind-direction "pegging". Some stations were discarded if they seemed inadequate. A total of seventeen stations are used to verify the model forecast. The 10-minute averaged data of station measurements are used to filter out high frequency noise and compare with the model prediction at the end of every simulation hour. The locations and detailed information of these stations are listed in Table 1 (also see Fig. 1). Note that the surface station measurements were made at different heights. Therefore, the verification is assessed at the corresponding or closest model grid heights. To overcome the restriction of coarser spatially distributed station data, tracer measurements of SF<sub>6</sub> from 100 NOAA samplers in the downtown area of the Salt Lake City (roughly 9 km x 9 km) are also used to assess the performance of UCP in the mesoscale model.

#### 3. URBAN CANOPY PARAMETERIZATION

## a. Urban Canopy Formulation

The building effect is parameterized in the horizontal direction in this UCP. In the vertical, we use very high grid resolution to calculate the rooftop effects within each urban canopy. The UCP used is based on Brown and Williams (1998), which was extended from Yamada's (1982) forest canopy scheme. In this study, additional modifications to BW's scheme are made to accommodate the model physics in COAMPS and to represent the urban canopy effects in a more consistent way. These modifications include the additions of building drag term in the vertical momentum equation

and rooftop surface energy equation, changes in the effects of anthropogenic heat and rooftop in the heat equation, and drag terms in the momentum equations.

The main differences of the urban canopy to the forest canopy are marked in two aspects; 1) the addition of anthropogenic heat source, and 2) further division of the urban canopy into the roof region and the between building (or called street canyon) area (Fig. 2).

As in the forest canopy, the urban canopy acts as a friction source in the momentum equations,

$$\frac{DU}{Dt} = \cdots - \text{froof} \cdot \text{cd} \cdot \text{a}(z) \cdot U \cdot |U|, \tag{1}$$

$$\frac{DV}{Dt} = \cdot \cdot \cdot - \text{froof} \cdot \text{cd} \cdot \text{a}(z) \cdot V \cdot |V|, \tag{2}$$

$$\frac{\mathrm{DW}}{\mathrm{Dt}} = \bullet \bullet \bullet - \mathrm{froof} \bullet \mathrm{cd} \bullet \mathrm{a}(\mathrm{z}) \bullet \mathrm{W} \bullet |\mathrm{W}|, \tag{3}$$

where  $f_{roof}$  is the horizontal fraction of model grid covered by the building regions of the urban canopy,  $c_d$  the drag coefficient of the urban canopy, and a(z) the building surface area density profile of the urban canopy. For simplicity, a linear configuration of the a(z) profile is used in this study (Fig. 3).

Distinct from the momentum equations, the urban canopy is treated as a source of turbulence production to account for turbulence wake generation in the turbulence kinetic energy (TKE) equation,

$$\frac{D(TKE)}{Dt} = \cdot \cdot \cdot + froof \cdot cd \cdot a(z) \cdot (|U|^3 + |V|^3 + |W|^3). \tag{4}$$

Unlike BW's scheme using  $f_{urb}$  in the momentum and TKE equations, the use of  $f_{roof}$  in these equations enables the modified urban parameterization to show more dependence of urban drag on the size of building region rather than on the street canyon portion.

The effect of the urban canopy on the heat equation is more complicated than the one shown in Yamada's forest canopy. The impacts of the urban canopy on the potential temperature equation is expressed by

$$\frac{D\theta}{Dt} = \cdots + \frac{1}{\pi \cdot \rho \cdot c_p} \cdot \{(1 - f_{urb}) \cdot \frac{\partial R_N}{\partial z} + f_{urb} \cdot \frac{\partial q_{urb}}{\partial z} +$$
(5)

$$(1 + \frac{1}{B})^{\text{-}1} \cdot [(f_{urb} \text{-} f_{roof}) \cdot \frac{\partial R_{Nc}}{\partial z} + f_{roof} \cdot b(z) \cdot \frac{\rho \cdot c_p \cdot \Delta q_{roof}}{C_{roof}}]\},$$

where  $R_N$  and  $R_{Nc}$  are the net downward radiative (LW+SW) fluxes in the rural and street canyon regions of the urban canopy, respectively,  $\pi$  non-dimensional pressure,  $\rho$  air density,  $c_p$  specific heat of dry air at constant pressure, B Bowen ratio of the urban canopy,  $C_{roof}$  heat capacity of the roof, and  $b(z_k)$  the normalized function of roof surface area density function, defined as  $\frac{a(z_k) \bullet dz_k}{\sum\limits_k a(z_k) \bullet dz_k}$ ,

where  $dz_k$  is the vertical grid depth within the urban canopy. The normalized function, b(z) is used to prevent the UCP from over-predicting the rooftop effects of nighttime warming and daytime cooling, respectively.

Equation 5 contains four physical terms; 1) the radiative heating/cooling term in the rural region, 2) the anthropogenic heating term in the urban region, 3) the radiative heating/cooling term in the street canyon region, and 4) the rooftop heating/cooling term in the urban region with buildings. All terms of concern have the same sign of diurnal cycle (i.e., nighttime cooling and daytime warming), except for the anthropogenic heating term using a temporally invariant value in this study. The consideration of Bowen ratio in Eq. 5 acts to weaken the cooling or warming of the street canyon and roof regions, as compared to their rural counterparts. Therefore, this UCP acts to simulate the urban effect of nighttime warming and daytime cooling (relative to the rural environment) when anthropogenic heating is weak as represented for this case study. Under the situation with weak anthropogenic heating, the urban impact is dominated by the rooftop effect in this UCP. When the anthropogenic heating is substantially large as seen in the major metropolitan cities, the rooftop effect of daytime cooling can be suppressed by the dominant anthropogenic heating, and lead to evident net daytime heating.

Another distinction from BW's heat equation is that a user-specified vertical profile of anthropogenic heat flux  $(q_{urb})$  is used within this urban canopy. For simplicity, a linearly decreasing profile of  $q_{urb}$ , similar to a(z), is adopted in this study. The Bowen ratio is assumed to be well mixed within the urban canopy as in BW's scheme.

The net radiative flux within the street canyon region is defined as,

$$R_{Nc}(z) = R_h^{\text{net}} \cdot \exp[-k \cdot L(z)], \qquad (6)$$

where  $R_h^{net}$  is the net downward total radiative flux at the top of the urban canopy, k a user-specified extinction coefficient, and L(z) the cumulative index of building surface area determined by

$$L(z) = \int_{z}^{h_c} a(z') \cdot dz', \qquad (7)$$

where h<sub>c</sub> is the height of the urban canopy top. Unlike Martilli's (2002) approach, the building wall effect to the street canyon of the urban environment is parameterized in a simple fashion, which is implicitly considered in Eq. 6. During the daytime, the building shadowing effect of solar radiation can cool the wall surface while the reflection of solar radiation by the other parts of building walls can still warm the atmosphere in the shadow portion of the street canyon. As the solar zenith angle becomes very small, this shadowing effect might be weak or even change sign. However, the time span of small zenith angle only occupies a small portion of the day. Therefore, the physical consideration of this simple parameterization of building wall effect is still valid for general applications. As a result, the sensible heat flux toward the wall surface can have a cooling effect in the air between the buildings during the day. In contrast, the stronger longwave cooling in the street canyon creates an opposite horizontal temperature gradient, which results in a warming effect in the air between the buildings at night.

Due to the weak heat flux in the insulated layer of the roof, the assumption of fully insulated roof bottom is made in this study. The heat flux change of the rooftop surface at each level of model grids within the urban canopy is, thus calculated by

$$\Delta q_{roof} = R_{SW}^{\downarrow} \cdot (1 - \alpha) + \varepsilon \cdot (R_{LW}^{\downarrow} - \sigma T^4) - \rho \cdot c_p \cdot c_{d\_roof} |V| \cdot (T_{roof} - T).$$
(8)

where  $R_{SW}^{\downarrow}$  and  $R_{LW}^{\downarrow}$  are the downward SW and LW radiative fluxes at the rooftop surface,  $\alpha$  roof albedo,  $\epsilon$  roof emissivity,  $c_{d\_roof}$  drag coefficient of roof surface, |V| and T ambient wind velocity and

temperature.  $T_{roof}$  is determined by the rooftop surface energy equation,  $\frac{\partial T_{roof}}{\partial t} = \frac{\Delta q_{roof}}{C_{roof}}$ .

The initial condition of  $T_{roof}$  is set to be the same as the air temperature of the same height. The sensitivity of initial rooftop temperature to the model solution is illustrated in Figure 4. Results indicate that the initial condition of rooftop temperature has trivial impact on the predicted air temperature although it exhibits noticeable impact on the rooftop temperature. This result is mainly due to the small rooftop sensible heat flux term in Eq. 8 along with the impact of Bowen ratio and smaller roof fraction in Eq. 5. Therefore, the assumption of initial rooftop temperature used in this study is fairly justified for practical applications.

The Equation (8) is, however, simplified in BW's scheme by assuming that the rooftop is infinitely thin and that all radiation absorbed by the roof is immediately re-emitted as LW radiation at the air temperature; i.e., the roof has no heat storage capacity. In contrast, the effect of roof heat capacity is considered in this study. The addition of rooftop surface energy equation enables the modified UCP to exhibit a more reasonable diurnal cycle of the heat island effect (Chin et al. 2000), which produces the nighttime warming with the maximum near sunrise and daytime cooling as observed in many field experiments (Garstang 1975; Oke 1982; Bornstein 1987). This modified UCP also result in stronger nighttime warming / daytime cooling with the increasing roof fraction.

Due to the larger heat capacity of rooftop, a larger roof fraction causes a greater time lag of the temperature rise after sunrise.

The impact of the urban canopy on the surface radiation budget is treated differently from its forest counterpart by assuming that the heat within the building portion of the urban canopy is released directly into the air aloft. Therefore, the anthropogenic and rooftop heating terms in the roof region are assumed to have no impact on the surface net total radiative flux ( $R_{N_G}$ ),

$$R_{N_G} = (1 - f_{urb}) \cdot (R_{SW}^{net} - R_{LW}^{net})_G + f_{cnyn} \cdot [R_{N_c}(0)]_G$$

$$(9)$$

and the surface energy equation,

$$\frac{\partial T_G}{\partial t} = R_{N_G} - H_G - L_G - S_G, \tag{10}$$

where  $T_G$ ,  $H_G$ ,  $L_G$ , and  $S_G$  are surface temperature, sensible heat flux, latent heat flux, and soillayer heat flux, respectively.

## b. Urban Canopy Parameters

Resulting from limited data to describe the urban characteristics, a major challenge for using an UCP in mesoscale models is to determine appropriate input parameters. To this end, different resolutions of the USGS land-use data sets are used in conjunction with the available urban infrastructure and urban surface properties to provide the required input information for the UCP. These land-use data, Land Use Land Cover (LULC) and National Land Cover Data (NLCD), have a resolution of approximately 200 m and 30 m, respectively. The 200-m data set (LULC) has a total of 37 land surface categories, including seven urban categories. The 30-m data set (NLCD) has 21 land-use categories in total, but with only three urban categories, covering high and low density residential, industrial and commercial areas. Therefore, the primary urbanization categories are not represented in the high-resolution (30-m) land-use data set (see Tables 2 and 3).

In this study, the urban surface properties of a given land-use category are assumed to exhibit universal characteristics. Therefore, every land-use category given from the USGS data set

determines corresponding urban surface properties via a table conversion approach. The urban surface properties of given land-use category shown in Tables 2 and 3 are based on available measurements (Anthes et al. 1987; Pielke 1984; Wilson et al. 1987; Stull 1988). As a result, the derived urban surface properties of all input land surface categories are used to determine the urban properties of each COAMPS grid point through the weighted average of land-use category occurrence frequency in each COAMPS grid domain.

Unlike the urban surface properties, the urban infrastructure properties for a given land-use category (e.g., building height and anthropogenic heating) may greatly vary from city to city. Urban infrastructure properties shown in Table 2 and 3 are based on the satellite aerial photo to estimate the urban and roof fraction information for the Salt Lake Valley. The urban canopy height and anthropogenic heating are estimated from actual building height and population information. Then, the urban infrastructure properties at the mesoscale grid can be derived in the same way as the surface properties via a table conversion approach. Further application of these urban infrastructure properties needs proper adjustment to fit the actual application for other geographic locations.

The derived urban infrastructure properties are assumed to be time-invariant parameters while the urban surface properties have seasonal variation based on the sine function from the winter and summer maximum or minimum values. Therefore, this table conversion approach acts to provide a database for the urban properties, which can be applied to any other geographic locations.

Figure 5 illustrates the differences of derived urban infrastructure parameters between two sets of USGS land-use data with different resolutions over the Salt Lake Valley in the third nest domain ( $\Delta x = 4$  km). The land-use data with lower resolution (200-m) show larger urban roof fraction, urban building height, and anthropogenic heat flux, and wider spatial definition of the urban zone. As described earlier, these differences are in great part attributed to extra urban categories in the

200-m land-use data. The differences of urban properties in the common categories of both landuse data sets also contribute to these differences (see Table 2 and 3).

The urbanization also impacts the surface properties (Fig. 6). Drier and rougher surfaces are shown in the populated urban land surface, particularly in the 200-m land-use data. Besides, both 200-m and 30-m data sets show clear improvement in the surface wetness over the Utah Lake and the Great Salt Lake regions as compared to the relatively coarse definition of surface wetness using the ETA analysis field.

Note that a missing land-use data zone exists in the lower right corner of 200-m data set in the third nest domain. These missing land-use data are caused by the undefined land surface categories. As a result, a block of constant values is seen in the derived surface properties, such as wetness and roughness (Figs. 6c and 6d). However, the primary sensitivity experiments of this study are performed with higher horizontal resolution ( $\Delta x = 1.33$  km) simulations in a smaller nest-4 domain (see Fig. 6a). Therefore, the higher resolution simulations are not influenced by this impact since the UCP is turned on only in the most inner model domain.

In addition to aforementioned parameters for the urban infrastructure and urban surface properties, other user specified constant parameters are needed for this urban canopy scheme. These constants include urban drag coefficient ( $C_d = 0.012$ ) and Bowen ratio for the urban canopy (B = 1.5); extinction coefficient of radiation flux in the street canyon (k = 0.1); rooftop LW emissivity ( $\epsilon = 0.91$ ); rooftop surface albedo ( $\epsilon = 0.22$ ), roof drag coefficient ( $\epsilon = 0.0071$ ); and roof heat capacity ( $\epsilon = 0.91$ );  $\epsilon = 0.0071$ ); and

As shown later, rooftop plays a dominant role on the simulated urban boundary layer. The impact of rooftop properties, such as albedo and emissivity to the model prediction is also included in the sensitivity experiments using larger albedo (0.37) and varied emissivity (1.0 and 0.8) to represent a typical albedo increase (0.15) by the white topping asphalt roof for SW radiation, and weaker and blackbody emission roof for LW radiation, respectively. The impact of rooftop

properties on the predicted air temperature is shown in Fig. 7. Results indicate that the increase of roof albedo by 0.15 effectively reduces the daytime roof temperature by up to 4 °C or so at the location with large urbanization (Fig. 7a) while its impact on the corresponding air temperature remains small due to combined influence of roof fraction (greatly less than 1; see Fig. 5a) and Bowen ratio (see Eq. 8). In contrast to the dominant term of SW flux, the weaker LW flux term is offset by the rooftop sensible heat flux term at comparable magnitude. Although the smaller emissivity of rooftop leads to the warming of rooftop temperature than its counterpart with the blackbody emission, the resulting predicted air temperature still shows trivial influence by the change of LW emissivity (Fig. 7b). Generally speaking, for this weak UHI case, the changes of rooftop SW and LW properties exhibit little impact on the prediction of the mesoscale simulation.

#### 4. Results

## a. Modeled Urban Impact on Near-Surface Fields

The urban impact on the model prediction is assessed by comparing model simulations with derived urban forcing using both resolutions of USGS land-use data (referred to as UCP\_30m and UCP 200m, respectively) and with the simulation without the urban forcing (no UCP).

Figure 8 shows the nighttime urban impact near the surface using the simulations with the urban effect derived from the 30-m land-use data, and without the urban effect. The urban canopy produces a nocturnal warming (relative to no\_UCP) along the urban zone in the Salt Lake Valley, with a maximum value of 1.8 °C at the level of 10 meters above the ground (Fig. 8a) and a corresponding hydrostatically-induced negative pressure anomaly zone (Fig. 8b). As seen in Eq. 5, this warming is a result of the weaker nighttime cooling within the urban canopy than its rural counterpart due to the urban heat release at night. The primary nighttime urban warming region and the associated negative pressure anomaly zone are shifted slightly to the downwind (west) side of the center zone of the urban area. This spatial shifting is in response to the advection effect of the strong drainage flow near the SLC downtown and the station QHW until it interacts with the

ambient southerly flow. Therefore, the dominant nighttime urban warming area resides within the wind deformation zone, which is located at the interface between the ambient southerly flow to the west and the mountain canyon drainage flow to the east.

The comparison of predicted nighttime 10-m winds between UCP\_30m and no\_UCP runs clearly exhibits three areas with noticeable differences (Fig. 8b). One is located at the eastern boundary of the dominant nighttime urban warming zone due to the building drag slowing down the drainage flow. As a result, the wind deformation zone in the no\_UCP run is slightly shifted to the west by a distance of one to two grids following the drainage flow. Another two locations at the southeast corner of the Great Salt Lake are attributed to the differences in surface roughness (Figs. 6b and 6f).

In contrast to the nighttime response, the modeled urban canopy exhibits a daytime cooling effect (relative to no\_UCP) on the low-level atmosphere (Fig. 9a), and the magnitude (< 1 °C) is weaker than the nighttime case. This diurnal variation of urban forcing (e.g., nighttime warming and daytime cooling) has been seen in many earlier field studies as described in the Introduction. Unlike the nighttime situation, the main urban infrastructure zone in the late afternoon is primarily influenced by the ambient wind from the southwest due to the absence of drainage flow. Thus, the urban canopy induced daytime cooling as well as the associated positive pressure anomaly is shifted to the downwind side of the dominant ambient wind (Figs. 9a and 9b). As in the nighttime situation, major daytime discrepancies in the near-surface wind field between the simulations using UCP\_30m and no-UCP runs are attributed to the urban drag and surface roughness.

The simulation of UCP\_200m exhibits stronger nighttime urban warming than its 30-m counterpart (Fig. 10a). The corresponding larger urban infrastructure parameters, described in Figure 5 exert more urban drag on the wind field (Fig. 10a). Therefore, there are noticeable differences in the wind field in the urban infrastructure zone between the simulations of UCP\_200m and UCP\_30m. As in the no\_UCP run, the larger surface roughness of 200-m land-use data in the

eastern branch of the Great Salt Lake has substantial impact on the near-surface winds. In general, the 30-m land-use data better represents the surface properties over the water areas. However, the 200-m data produce stronger urban thermal and mechanical forcing primarily due to the more inclusive categorization of urban land surface than the 30-m land-use data. The daytime impact of urban forcing derived from varied resolutions (30-m vs. 200-m) of land-use data resembles its nighttime counterpart, except for the opposite sign of the urban forcing (Figs. 10a and 10b).

As a whole, the urban zone of IOP-10 is located at the interface of two flow regimes; the ambient southerly flow prevails all day long to the west, and the down- and up-valley flow to the east as a result of the variation of surface energy budget on the mountain slope. Unlike the other IOPs, the meso-net observations in the Salt Lake Valley show that the prevailing land-lake breeze did not appear in IOP-10 to influence the urban zone. The absence of this mesoscale flow may be due to the synoptic condition described in section 2a. The movement of simulated urban nighttime warming / daytime cooling core with the dominance of drainage / ambient southerly flow clearly suggests that the diurnal variation of predicted urban forcing and winds over the Salt Lake Valley exhibits strong interactions between synoptic, mountain and urban scales in IOP-10.

## b. Modeled Urban Impact on the Low-level Atmosphere

The drainage flow at the western slope of the Wasatch Mountains is clearly identified at night in the no\_UCP simulation (Fig. 11a). As a result of LW cooling, this low-level cold air can propagate westward across the Salt Lake Valley. As the UCP is turned on, the nocturnal urban forcing acts to heat the urban canopy (Fig. 11b). Thus, the cold air tongue retreats substantially in the simulations with the UCP. In contrast, the up-valley wind appears during the daytime, and the UCP exerts an opposite effect to cool the urban canopy (Figs. 11c and 11d) while the magnitude is weaker than its nighttime warming counterpart.

Figure 12 show the evolutions of vertical profiles of predicted temperature from the simulations with and without the urban effect at the COAMPS grid point nearest the station M04 (see Fig. 1).

This station is selected by the fact that the largest roof fraction and anthropogenic heating is located near this grid point (see Table 1). Without the urban impact, the no\_UCP simulation shows a clear nighttime low-level inversion layer above the surface (Fig. 12a). With the urban canopy parameterization turned on, the temperature inversion becomes weakened in the urban area. However, the inversion layer structure still exists in most of the model domain, except for some locations near the station M04, which has the largest derived roof fraction of urbanization. For the simulations with the urban forcing, an elevated inversion layer starts to appear above a nearly neutral surface layer at 26 hours of UCP simulations (i.e., one hour after sunrise), and lasts for only two hours (Figs. 12b and 12c). The delay and the short persistence time of the elevated inversion layer in this case is due in great part to the weaker urban nocturnal heating, which is involved in a complicated interaction among urban infrastructure, local topography and strong ambient wind. The lingering of nocturnal heat island effect can also impact other types of scale interaction. Yoshikado (1992) reported an analogous situation for the delay of sea breeze progression.

In this study, the top of the modeled urban canopy at the station M04 resides at 9 and 18 meters above the ground for the 30-m and 200-m resolutions of land-use data, respectively while the temperature response of the urban canopy at night can reach higher altitudes due to the enhanced turbulence transport of heat (see Fig. 13). The depth of the predicted nocturnal urban boundary layer (22 and 36 meters for UCP\_30m and UCP\_200m, respectively) is nearly twice the urban canopy height for this weak heat island case. A similar finding was reported in an earlier field study (Uno et al. 1988).

It is interesting to point out that the ratio of the modeled urban boundary layer height to the urban canopy height is nearly constant in spite of the height of the urban canopy. This result substantially differs from a recent two-dimensional modeling study by Martilli (2002), which exhibits a varying ratio for a range of urban canopy heights. The ratio in Martilli's study roughly ranges from five to eight; the larger the urban canopy height, the smaller the ratio is. These ratios

seem higher than those of earlier field studies, which showed a ratio of three to four for the urban cities of the metropolitan size (Duckworth and Sandberg 1954; Bornstein 1968). It is also interesting to note that the top of nocturnal inversion layers shown in the no\_UCP run is barely influenced by the addition of urban forcing although its base height evolves with the intensity of modeled UHI. This suggests that the top of the elevated inversion layer is mainly determined by the LW cooling of the large-scale environment.

Figure 14 depicts the impact of UCP on the horizontal wind field near the station M04. A clear diurnal cycle of valley winds is identified in both no\_UCP and UCP simulations. The predicted low-level nocturnal jet at 27 hours of the no\_UCP simulation, located near 30 meters above the ground (not shown) is elevated by about 20 meters in the UCP\_200m run (Fig. 14a). This elevated jet-like wind profile is in response to the enhanced low-level TKE (Fig. 13) from the combined urban heat island (buoyancy) and urban drag (mechanic) effects. As a result, the vertical transport of momentum by turbulence modifies the horizontal velocity field by slowing down / accelerating the layer below / above 60 meters (Fig. 14b). This urban impact is stronger in the 200-m run than in the 30-m simulation (Fig.14c) mainly due to the larger urban forcing in the 200-m land-use data.

Another interesting result is the direction of wind shift by the urban impact. A noticeable wind direction shift of ~20° clockwise near the surface is identified in the predicted afternoon wind profile with the UCP (33 hours of simulation in Fig. 14b) while a weaker wind shift of 10° or so counter-clockwise is seen in the nighttime (21 hours of simulation time). A similar urban wind shift effect has been reported in earlier field studies (Angell et al. 1971; Draxler 1986). Based on the urban thermally induced pressure perturbation (see Figs. 8b and 10b), this factor cannot explain the direction of predicted nighttime and daytime urban wind shift in this weak UHI case. Simulations, however, suggests clear correlation of this wind shift effect to the orientation of local terrain.

## c. Sensitivity to the Urban Canopy Parameterization

In most of the simulations described in this paper, the model resolution was set to 1.33 km. To test the effects of the coarser model resolution, a simulation with the horizontal resolution of 4 km was conducted. Results from the coarser resolution of UCP\_30m simulation (Fig. 15) are compared with the parallel results from the finer resolution run (Fig. 8). There are considerable but consistent differences in both the temperature and wind fields. In both cases, the maximum temperature change is centered over the urban area of Salt Lake City. However, the maximum values of those changes are greater in the finer resolution simulation and their gradients are steeper, reflecting a more concentrated zone of urban influence. The wind field response is consistent with the temperature field. The wind prediction shows a local minimum over the urban zone where the temperature change is a maximum, as the winds respond to the thermal forcing and roughness effects. Hence, it is concluded that the coarser model resolution leads to weaker urban forcing, which produces weaker turbulence (Figs. 16b and 13c). As a result, a well-defined nocturnal urban boundary layer with an elevated inversion aloft does not form in the coarser resolution simulation although the surface inversion layer is substantially weakened (Figs. 16a and 12c). Similar results also appear in the UCP\_200m simulations (not shown).

The effects of no anthropogenic heating appear to be minimal (Fig. 17a and 12b). This is not surprising since the prescribed anthropogenic heating is small (< 30 W m<sup>-2</sup>). In contrast, when urban surface properties are not defined in the UCP, a nocturnal urban boundary layer still develops in response to the urban infrastructure parameters alone (Fig. 17b). Finally, when including urban surface properties but excluding urban infrastructure effects, no elevated inversion layer forms and the urban effects are minimal (Fig. 17c).

According to these sensitivity studies, the combined effects of street canyons and building rooftops show the most pronounced influence on the urban boundary layer properties. Further sensitivity study indicates that the street canyon effect is much weaker than its rooftop counterpart in this UCP. As a result, the sensitivity experiment without the street canyon effect (not shown)

still exhibits an elevated inversion layer as seen in Figs. 17a and 17b. Therefore, the rooftop effect is the dominant contributor to the thermal field in this simulated urban boundary layer.

## d. Model Verification with Surface Station Data and Tracer Measurements

To validate the urban impact in the mesoscale model, simulations are evaluated using standard meteorological station measurements and SF6 tracer data. The root-mean-square errors (RMSE) of the predicted near-surface wind direction, wind speed, and temperature are presented in Figure 18. These RMSEs are calculated with respect to the data obtained from Utah meso-net, VTMX 2000, and Urban 2000 stations using the results at every forecast hour over the entire simulation period of 36 hours. The stations chosen are ordered such that lower station numbers correspond to smaller amounts of roof fraction; i.e. urbanization increases in the positive x-direction.

Note that some of observational data are removed from the RMSE calculations. These removed data are related to the situation with near calm wind when the wind direction is highly variable. This data removal acts to minimize the impact of uncertain measurements on the RMSE calculations when the difference of wind direction between observation and simulation is greater than 90 degrees and the observed wind is less than 1 m/s. As a whole, the number of removed samples is less than 10% of the total hours among stations with a typical number less than 3; however, they can substantially increase RMSE and contaminate the signal on detecting the wind shift by the urban effect.

It is clear from the wind direction trace that higher RMSEs appear at the stations with larger roof fraction (Fig. 18a). The difference of RMSEs between non-urban and urban runs tends to be small at the stations with lower roof fractions while this magnitude increases in the areas with larger urban impact. Although the UCP has an effect to reduce the RMSE of wind direction, the magnitude is much smaller than the total RMSE. This suggests a possibility that the single-station observations are not representative of the urban area equivalent to the mesoscale grid size, and the magnitude of RMSEs in this condition cannot be regarded as the measure of the forecast error since

the measurements from the urban environment are subject to great local building influence. Therefore, further observational evidence and modeling studies are necessary to substantiate this conclusion.

In contrast to the wind-direction traces, wind-speed RMSEs do not exhibit clear dependence on urbanization (Fig. 18b). However, the RMSE is reduced with increasing urbanization as a result of increased urban drag in the simulations with the UCP. On the other hand, temperature forecasts show resemblance of close dependence on urbanization, i.e. increased RMSE in the areas with larger roof fraction (Fig. 18c). This outcome is consistent with the stronger nighttime urban warming and weaker daytime cooling in the simulations with small anthropogenic heating. Therefore, net urban warming is expected in the RMSE calculations.

Time sequences of the wind direction traces for 36-hour forecasts from selected stations are presented in Figure 19. The plots are ordered such that letters earlier in the alphabet depict stations with a greater amount of urbanization. Hence, the station MO4 has the greatest amount of urbanization, and station UT5 the least. In general, the comparisons show increased agreement between the observed quantities and the simulations as the urbanization decreases. One exception is station MO4, which is located at the eastern edge of the Salt Lake City urban core (see Fig. 1). Station UT5 is outside the urban core, but also to the east of the city. This is an area that is affected by strong drainage flow off the Wasatch Mountains to the east of the city core. At both station MO4 and UT5, the nocturnal easterly to northeasterly drainage flow is well forecasted, but the afternoon up-valley, westerly and northwesterly flow is not well predicted. This discrepancy can be partially explained by the urban effects. The modification of the wind direction by the drag and thermodynamic effects depends on the travel distance in the urban area. During the night, station MO4 and UT5 are effectively upwind of the urban core, while during the day they are downwind.

The UCP exerts a direct influence on the wind speed through the drag term in the momentum equation. Therefore, lower wind speeds are forecasted with the UCP than without it, particularly at

locations with larger roof fraction (Fig. 20). The comparison of wind speeds exhibits substantial differences between the predicted and observations. In the higher urbanization areas, observed winds tend to be weaker than the model forecasts at the stations from URBAN 2000 (e.g., Figs. 20d and 20e), and stronger in the areas from the VTMX meso-net, particularly at night (e.g., Figs. 20b and 20c). Typically, an urban environment consists of buildings and street canyons, paved and concrete surfaces, other urban structures and some rural areas. The footprint of immediate surroundings most likely biases individual station observations, making them problematic for the mesoscale model validation.

The temperature predictions generally agree with observations better than the wind forecasts. However, noticeable discrepancies exist at the urban locations during two time segments through the 36-hour period: the nocturnal drainage flow period and the second daytime peak near the end of the period (Fig. 21). The difference at night mainly arises from the modeled nighttime urban warming from the rooftop effect. This effect is not properly reflected in the surface based observations. The other daytime difference is due to the higher simulated cloudiness leading to the under-prediction of the second daytime temperature peak at all stations shown.

Generally speaking, these comparisons clearly demonstrate the limitations of using single-station data to evaluate the performance of UCP in the urban areas. However, nighttime SF6 tracer data at relatively high spatial density collected during the URBAN 2000 experiment are very useful for this purpose.

Using the tracer data for validation, simulations with the UCP substantially improve the plume forecasts (Fig. 22). The predicted nighttime plume using the UCP forecast shifts 20-30 degrees to the right, and is consistent with the wind shift seen in the wind direction predictions shown in the urban areas of site BB and BG at earlier morning hours (Figs. 19d and 19e). This urban effect on the plume prediction and wind direction forecast is consistent with the finding of earlier studies (Angell et al. 1971; Draxler, 1986). The better agreement of UCP simulations with tracer

concentration data than single station measurements also supports the wind speed forecast, as concentration transports away from the source more quickly without the UCP. However, there are trivial differences in the plume forecasts using different resolutions of land-use data sets.

As a whole, the model predicts an average or integrated wind vector to transport and disperse the tracer. The observed tracer is also an averaged quantity, integrated over the length of time (generally one hour) that tracer was being released and integrated over the source-receptor distance. Small scale perturbations in the local wind fields or micro-scale wind patterns, such as eddies in the lee sides of buildings, affect the local observations, but those effects are averaged out in the integration as the tracer is transported from source to receptor. Therefore, we believe that our results demonstrate that the UCP improves mesoscale model forecasts in urban areas.

## 5. Summary and Discussion

With the addition of the rooftop surface energy equation and additional changes, we present a modified version of Brown and Williams' (1998) urban canopy parameterization (UCP) to more realistically simulate the urban impact in the mesoscale model. Multiple resolutions of USGS landuse data are also utilized to derive urban infrastructure and urban surface properties as the inputs to drive the UCP. This UCP is used to assess the urban impact on surface and lower atmospheric properties using COAMPS. The intensive observational period with clear-sky, strong ambient wind and drainage flow, and the absence of land-lake breeze over the Salt Lake Valley, occurring on 25-26 October 2000, is selected for this study. Both conventional surface station measurements and tracer concentration observations are used to gauge the performance of UCP for the sub-grid building effect in the mesoscale model.

Results indicate that under the selected urban environment, urban surface characteristics and anthropogenic heating plays little role in the formation of the simulated nocturnal urban boundary layer. This outcome agrees with an earlier remark on the effect of anthropogenic heating on the genesis of UHI in most cities (Oke 1995). The main contributor to this urban boundary layer is

attributed to the building rooftop effect. Sensitivity test also shows that the model horizontal grid resolution is important in simulating the elevated inversion layer for this weak UHI case.

The results using derived urban properties from different resolutions of USGS land-use data indicate that the coarser resolution (200 m) data set leads to a stronger urban forcing than the finer resolution (30 m) case mainly due to extra urban land categories considered in the coarser resolution data. Nonetheless, the higher resolution of land-use data has a better improvement on the surface properties over the local lakes. Sensitivity experiments further reveals that the depth of the predicted urban boundary layer is about twice the urban canopy height in this weak UHI case, and that this ratio is nearly constant despite the type of land-use data used. The same ratio was reported in an earlier field study (Uno et al. 1988). However, a higher ratio of three to four was also observed in the cities of the metropolitan size (Duckworth and Sandberg 1954; Bornstein 1968).

The root mean square errors of predicted wind and temperature with respect to the surface station measurements exhibit fairly large discrepancies at the urban locations. However, the close agreement of modeled tracer concentration with observations fairly justifies the modeled urban impact on the wind direction shift and wind drag effects. This result further confirms the finding of an earlier observational study regarding the inappropriate representative of single-station measurements to the urban environment (Draxler 1986). Generally speaking, our results indicate that the consideration of both thermal and mechanic aspects of sub-grid building effects in the mesoscale model is of importance for a better wind forecast in the urban areas.

The use of single-station measurements for the validation of the mesoscale model can cause substantial bias to the model forecast. However, this bias may be reduced by the measurements from multiple stations, which can represent different portions of the surrounding urban environment. Thus, the weighting average of multiple-station measurements may have more value to verify the urban impact in the mesoscale model. The consideration of this problem in the future field studies would be very helpful for the improvement of urban modeling work. Finally, results of

this study are based on simulations of a particular case, and cannot necessarily be applied to all urban environmental conditions. More case studies, representing a variety of urban conditions, should be conducted to generalize these urban effects. Further validation of UCP for the other five IOPs of URBAN 2000 with tracer data have been done, and will be reported in a separate article. In addition, the validation of UCP for other geographic location, such as the Oklahoma City (URBAN 2003) under quite different synoptic condition is our ongoing work toward this effort.

Acknowledgments. The authors wish to thank NRL for providing us the COAMPS model to test the urban canopy parameterization, and the journal reviewers for their valuable comments. We also thank the Department of Energy (DOE) Environmental Meteorology, and Chemical and Biological National Security Programs for using VTMX 2000 and URBAN 2000 data to validate the model results, and the DOE National Atmospheric Release Advisory Center for the computational resource. This work was supported by the DOE Chemical-Biological National Security Program and conducted under the auspices of the U.S. DOE by the University of California, Lawrence Livermore National Laboratory under Contract W-7405-Eng-48.

### References

- Akima, H., 1978, A method for bivariate interpolation and smooth surface fitting for irregularly distributed data points: ACM Trans. on Mathematical Software, 4, no. 2, pp. 148-159.
- Allwine, K. J., J. H. Shinn, G. E. Streit, K. L. Clawson, and M. Brown, 2002: Overview of URBAN 2000. *Bull. Amer. Meteor. Soc.*, **83**, 521-536.
- Angell, J. K., D. H. Pack, C. R. Dickson, and W. H. Hoecker, 1971: Urban influence on nighttime airflow estimated from Tetroon flights. *J. Appli. Meteorol.*, **10**, 194-204.
- Anthes R. A., E-Y. Hsie, and Y-H. Kuo, 1987: Description of the Penn State/NCAR Mesoscale Model Version 4. NCAR Technical Note, NCAR/TN-282+STR, National Center for Atmospheric Research, Boulder, Colo., 66 pp.
- Bornstein, R. A., 1968: Observations of the urban heat island effects in New York City. *J. Appl. Meteor.*, 7, 575-582.
- Bornstein, R. A., 1987: Mean diurnal circulation and thermaldynamic evolution of urban boundary layer. *Modeling the urban boundary layer*. Amer. Meteorol. Soc., Boston, 53-93.
- Brown, M. J. and M. Willams, 1998: An Urban Canopy Parameterization for Mesoscale Meteorological Models. *Proceedings of the AMS Conference on 2<sup>nd</sup> Urban Environment Symposium*, 2-7 November, 1998, Albuquerque, New Mexico, Amer. Meteor. Soc., 144-147.
- Carbone, R. E., 2000: Atmospheric observation in weather prediction. Storms, Vol. 1, R. A. Pielke and R. A. Pielke Sr., Eds., Routledges Press, 109-125.
- Chin, H.-N. S., M. J. Leach, and M. J. Brown, 2000: A preliminary study of the urban canopy effects on a regional-scale model: Sensitivity assessment of an idealized case. *Proceedings of the third Symposium on the Urban Environment*, July 14-18, 2000, Davis, California, Amer. Meteor. Soc., 76-77.

- ----, M J. Leach, G. A. Sugiyama, and F. J. Aluzzi, 2001: A Preliminary study of surface temperature cold bias in COAMPS. *Proceedings of the Nonth Conference on Mesoscale Processes*, 30 July 2 August, 2001, Fort Lauderdale, Florida, Amer. Meteor. Soc., 249-254.
- ----, M. L. Leach, J. M. Leone jr., G. A. Sugiyama, and H. Walker, 2002: Urban effect in numerical models and evaluation with field experiment data. *Proceedings of the fourth Symposium on the Urban Environment*, May 20-24, 2002, Norfolk, Virginia, Amer. Meteor. Soc., 39-40.
- Ching, J. K., J. F. Clarke, and J. M. Godowitch, 1978: The variability of the heat flux and mixed layer depth over St. Louis, MO. *WMO Symp. Boundary Layer Applied to Special Problems of Air Pollution*, Norkopping, Sweden, World Meteor. Org., 71-78.
- Clarke, J. F., 1969, Nocturnal urban boundary layer over Cincinnati, Ohio, *Mon. Wea. Rev.*, **97**, 582-589.
- Davies, H. C., 1976: A lateral boundary formulation for multi-level prediction models. *Quart. J. Roy. Meteor. Soc.*, **102**, 405-418.
- Draxler, R. R., 1986: Simulated and observed influence of the nocturnal heat island on the local wind field. J. Climate and Appl. Meteorol. Soc., 25, 1125-1133.
- Duckworth, F. S., and J. S. Sandberg, 1954: The effect of cities upon horizontal and vertical temperature gradients. *Bull. Amer. Meterorol. Soc.*, **35**, 198-209.
- Ermak, D.L., and J.S. Nasstrom, 2000: A Lagrangian stochastic diffusion method for inhomogeneous turbulence, *Atmos. Environ.*, **34**, 1059-1068.
- Garstang, M., P. D. Tyson, and G. D. Emmitt, 1975: The structure of heat islands, *Rev. of Geophysics and space physics*, **13**, 139-165.
- Hildebrand, P. H., and B. Ackerman, 1984: Urban effects on the convective boundary layer. *J. Atmos. Sci.*, **41**, 76-91.
- Hodur, R., 1997: The Naval Research Laboratory's coupled ocean-atmospheric mesoscale prediction system (COAMPS). *Mon. Wea. Rev.*, **125**, 1414-1430.

- Martilli A., 2002: Numerical study of urban impact on boundary layer structure: Sensitivity to wind speed, urban Morphology, and rural soil moisture. *J. Appli. Meteorol.*, **41**, 1247-1266.
- Morris, C. J. G., and I. Simmonds, 2001: Quantification of the influences of wind and cloud on the nocturnal urban heat island of a large city. *J. Appl. Meteor.*, **40**, 169-182.
- Oke, T. R., 1973: City size and the urban heat island. *Atmos. Environ.*, 7, 769-779.
- ----, 1982: The Energetic basis of the Urban heat island, Quart. J. Royal Meteor. Soc., 108, 1-24.
- ----, 1995: The heat island of the urban boundary layer: Characteristics, causes and effects. *Wind Climate in Cities*, J. E. Cermak et al., Eds., NATO ASI Series E, Vol. 227, Kluwer Academic, 81-107.
- Pielke, R. A., 1984: Mesoscale Meteorological Modeling. Academic Press, New York, 612 pp.
- Shreffler, J. H., 1978: Detection of centripetal heat-island circulations from tower data in St. Louis. *Bound.-Layer Meteor.*, 15, 229-242.
- Stull R. B., 1988: An introduction to boundary layer Meteorology. Kluwer Acad., 666 pp.
- Summers, P. W., 1965: An urban heat island model its role in air pollution problems, with application to Montreal. *Pres: First Canadian Conf. on Micrometeorology*, Toronto, ON, Canada.
- Uno, I., S. Wakamatsu, H. Ueda, and A. Nakamura, 1988: An observational study of the structure of the nocturnal urban boundary layer. *Bound.-Layer Meteor.*, **45**, 59-82.
- Wilson, M. F., A. Henderson-Sellers, R. E. Dickinson, and P. J. Kennedy, 1987: Investigation of the sensitivity of the land surface parameterization of the NCAR community climate model in regions of tundra vegetation. *J. Climatol.*, **7**, 319-343.
- Yamada, T., 1982: A numerical model study of turbulent airflow in and above a forest canopy. *J. Meteor. Soc. Japan*, **60**, 439-454.
- Yoshikado, H., 1992: Numerical study of the daytime urban effect and its interaction with the sea breeze. *J. Appli. Meteorol.*, **31**, 1146-1164.

## **Figure Captions**

- Fig. 1. Terrain height of the model nest-4 domain in unit of meter. The letters mark the locations of surface stations used in this study (see Table 1). The black line across the station M04 indicates the location of x-z cross-sections shown in this study. To avoid the overlapping of location labels at station BB, BG, and QB, only the station BG is shown in the figure.
- Fig. 2. Two dimensional view of the urban grid configuration in the horizontal and vertical directions. The urban canopy fraction  $(f_{urb})$  is further divided into roof fraction  $(f_{roof})$  and between-building (or called street canyon) fraction  $(f_{cnyn})$ . The area fraction in the rural region is defined as  $1 f_{urb}$ . The actual application is in three dimensions.
- Fig. 3. The building surface area density profile of the urban canopy in this study is assumed linearly decreased from the surface to the top of the highest building (i.e., the height of the urban canopy, h<sub>c</sub>).
- Fig. 4. Time series of model predicted 2-m air temperature (solid cells) and its corresponding roof temperature (open cells) at the station QHW (see Fig. 1) at every hour throughout the UCP\_30m simulation with the resolution of 4 km. Squared cells are for the run with the initial roof temperature same as the air temperature, diamond cells for the simulation with colder initial roof temperature by 10 °C, and circle cells for the run with warmer initial roof temperature by 10 °C.
- Fig. 5. Horizontal cross-sections of urban infrastructure properties derived from different resolutions of the USGS land-use data over the nest-3 domain ( $\Delta x = 4$  km). The left and right panels are for 200-m and 30-m resolutions, respectively. The plots from the top to the bottom are for roof fraction, canopy building height and anthropogenic heating, respectively. The contour lines represent the local terrain heights. The small box in (a) marks the nest-4 domain ( $\Delta x = 1.333$  km).
- Fig. 6. As in Fig. 5, except for the urban surface properties for ground wetness (left) and roughness (right column), and for varied choices of surface data sources (ETA-40km, UCP\_200m, and UCP\_30m from top to bottom, respectively).

- Fig. 7. As in Fig. 4, except for the sensitivity experiments with the rooftop properties having higher albedo (0.37) and varied emissivity (1.0 and 0.8, respectively). (a) the rooftop temperature at 2 meters above the ground, and (b) 2-m air temperature.
- Fig. 8. Horizontal cross-sections of 10-m nighttime forecasts at the 24 hours of the simulation time (i.e., 06h MST, October 26 2000) for the nest-4 domain of the UCP\_30m run. (a) Horizontal wind vector and temperature deviation, subtracted from the one in the no\_UCP run, and (b) the deviations of horizontal wind and pressure fields defined in the same as (a). Contour lines represent the local terrain heights.
- Fig. 9. As in Fig. 8, except for the deviations of 10-m forecasts for horizontal wind and temperature fields. The deviation is defined in the same way as Fig. 8, except for the differences between UCP\_30m and UCP\_200m. (a) 24 hours of forecast (06h MST, October 26 2000), and (b) 36 hours of forecast (18h MST, October 26 2000).
- Fig. 10. As in Fig. 8, except for the daytime forecasts of the UCP\_30m run at 36 hours of the simulation time (18h MST, October 26 2000).
- Fig. 11. Vertical cross-sections of forecast fields along the line across the station M04 as shown in Fig. 1. Top and bottom panels are for the nighttime (22 hours of simulation time; 04h MST, October 26 2000) and daytime (34 hours of simulation time; 16h MST, October 26 2000) forecasts, respectively. The wind vectors are plotted for no\_UCP (left) and UCP\_200m (right) simulations in terms of (u, w) components. The vertical wind is enlarged by 10 times to amplify the valley flow. The shading on the left panels is for the temperature forecast of no\_UCP run while the difference of temperature forecast between UCP\_200m and no\_UCP simulations is shown in the right panels.
- Fig. 12. Evolutions of the vertical profiles for the predicted temperature fields in unit of °C at the model nest-4 grid near the station M04. The curves on the plots are labeled by the forecast time (hour) of the simulation in an interval of 6 hours. The local time (MST) of each labeled forecast time is also shown in the parenthesis. (a) for the no\_UCP run, (b) for the UCP\_200m run, and (c) for the UCP\_30m run.
- Fig. 13. As in Fig. 12, except for the turbulence kinetic energy field in unit of m<sup>2</sup> s<sup>-2</sup>.

- Fig. 14. Evolutions of the vertical profiles for the predicted horizontal winds at the model nest-4 grid near the station M04. (a) for the UCP\_200m run, (b) for the deviation between UCP\_200m and no\_UCP, (c) for the deviation between UCP\_200m and UCP\_30m.
- Fig. 15. As in Fig. 8, except for the model nest-3 grid domain.
- Fig. 16. As in Figs 12a and 13c, except for the nest-3 grid of the UCP\_30m run.
- Fig. 17. As in Fig. 12b, except for different urban morphology. (a) no anthropogenic heating, (b) without using land-use data derived urban surface properties, (c) without using land-use data derived urban infrastructure properties.
- Fig. 18. Root mean square errors (RMSEs) of 36-h forecasts with respect to the surface station measurements for the nest-4 simulations with different configurations of urban properties at selected stations. The stations are labeled in sequence based on the size of roof fraction as shown in Table 1.
- Fig. 19. Evolutions of predicted wind directions throughout 36 hours of the nest-4 simulations at selected surface stations. The instruments of these stations are located at different heights ranging from 2 to 15 meters. The comparison of prediction with observation is made using the value at the closest model grid height. The plots are labeled in sequence based on the size of roof fraction. The locations and the details of these surface stations are shown in Table 1.
- Fig. 20. As in Fig. 19, except for the wind speed comparison.
- Fig. 21. As in Fig. 19, except for the temperature comparison.
- Fig. 22. Horizontal cross-sections of hourly-averaged modeled (contour) and observed (color bar) surface SF<sub>6</sub> concentrations in unit of parts per billion. The simulated concentrations are calculated using LLNL's Lagrangian Operational Dispersion Integrator based on COAMPS's prediction without and with the urban canopy parameterization for varied resolutions of landuse data. The pictures are shown at the second and fourth hours from the tracer release times, which correspond to 21 and 23 hours of simulation time in the COAMPS forecast. The plus sign shown in (b) marks the locations of NOAA samplers with tracer data.

Table 1. List of surface stations used in this study. These stations are labeled in order based on the size of derived roof fraction from the USGS 30-m land-se data. The station names are in convention of VTMX 2000 and URBAN 2000, except for the Blue Goose (BG). The locations, instrument heights, and station elevations are also included.

Sta #	Sta name	Source	Longtude	Latitude	Inst Height	Sta terrain	Roof fraction
1	QSA	Mesonet	-112.0100°	40.8300°	12 m	1283.0 m	0.0
2	QHE	Mesonet	-112.0200°	40.5200°	12 m	1475.0 m	0.0393
3	BLUF	Mesonet	-111.9783°	40.5727°	6 m	1420.0 m	0.0642
4	M01	PNNL	-111.9367°	40.5517°	1.5 & 3 m	1349.0 m	0.1098
5	UT5	Mesonet	-111.8010°	40.7122°	12 m	1743.0 m	0.1440
6	HQ2	Mesonet	-111.9596°	40.7267°	12 m	1250.0 m	0.1546
7	QMG	Mesonet	-112.0947	40.7061°	15 m	1323.0 m	0.1868
8	SLC	Mesonet	-111.9700°	40.7800°	10 m	1288.0 m	0.2008
9	BB	DPG	-111.8881°	40.7619°	5.2 m	1300.0 m	0.2503
10	BG	LLNL	-111.8813°	40.7586°	7.8 & 7.3 m	1306.0 m	0.2622
11	QB	DPG	-111.8853°	40.7666°	4.3 m	1308.0 m	0.2684
12	QCW	Mesonet	-111.8497°	40.6445°	12 m	1323.0 m	0.3040
13	QBT	Mesonet	-111.8822°	40.8965°	12 m	1323.0 m	0.3109
14	HOL	Mesonet	-111.8259°	40.6756°	2 m	1402.0 m	0.3204
15	M07	PNNL	-111.8552°	40.5833°	1.5 & 3 m	1435.0 m	0.3300
16	QHW	Mesonet	-111.8720°	40.7344°	12 m	1311.0 m	0.3310
17	M04	PNNL	-111.8238°	40.7124°	1.5 & 3 m	1406.0 m	0.3528

Table 2. Description of land-use categories based on the 200-m resolution of USGS data and physical parameters for winter and summer.

USGS LULC	f_urban	f_roof	h_urban	q_urban	albd_win	albd_sum	gwet_win	gwet_sum	z <sub>0</sub> _win	z <sub>0</sub> _sum
Residential	1.0	0.33	10 m	20 W/m**2	0.18	0.18	0.2	0.1	0.2 m	0.2 m
Commercial Service	1.0	0.25	25 m	25 W/m**2	0.18	0.18	0.1	0.05	0.6 m	0.6 m
Industrial	1.0	0.2	15 m	15 W/m**2	0.18	0.18	0.1	0.05	0.3 m	0.3 m
Communication	1.0	0.2	15 m	15 W/m**2	0.18	0.18	0.1	0.05	0.3 m	0.3 m
Industrial_Commercial	1.0	0.25	25 m	25 W/m**2	0.18	0.18	0.1	0.05	0.6 m	0.6 m
Mixed urban	1.0	0.25	20 m	20 W/m**2	0.18	0.18	0.1	0.05	0.5 m	0.5 m
Other Urban	1.0	0.5	50 m	50 W/m**2	0.18	0.18	0.1	0.05	2.0 m	2.0 m
Cropland_Pasture	0	0	0	0	0.25	0.21	0.6	0.3	0.06 m	0.18 m
Orchard_Vineyard	0	0	0	0	0.23	0.18	0.6	0.3	0.07 m	0.2 m
Confined Feeding	0	0	0	0	0.21	0.15	0.6	0.3	0.003 m	0.1 m
Other Agricultural Land	0	0	0	0	0.23	0.19	0.6	0.3	0.005 m	0.15 m
Herbaceous Rangeland	0	0	0	0	0.23	0.19	0.3	0.15	0.1 m	0.12 m
Shrub_Bush Rangeland	0	0	0	0	0.23	0.19	0.3	0.15	0.1 m	0.12 m
Mixed Rangeland	0	0	0	0	0.23	0.19	0.3	0.15	0.1 m	0.12 m
Deciduous Forest Land	0	0	0	0	0.17	0.16	0.6	0.3	0.5 m	0.5 m
Evergreen Forest Land	0	0	0	0	0.12	0.12	0.6	0.3	0.5 m	0.5 m
Mixed Forest Land	0	0	0	0	0.14	0.14	0.7	0.35	0.5 m	0.5 m
Stream_Canal	0	0	0	0	0.08	0.08	1.0	1.0	0.0001 m	0.0001 m
Lake	0	0	0	0	0.08	0.08	1.0	1.0	0.0001 m	0.0001 m
Reservoir	0	0	0	0	0.08	0.08	1.0	1.0	0.0001 m	0.0001 m
Bay_Estuary	0	0	0	0	0.08	0.08	1.0	1.0	0.0001 m	0.0001 m
Forested Wetland	0	0	0	0	0.14	0.14	0.7	0.35	0.4 m	0.4 m
Non-forested Wetland	0	0	0	0	0.14	0.14	0.75	0.5	0.2 m	0.2 m
Dry Salt Flat	0	0	0	0	0.3	0.3	0.1	0.05	0.002 m	0.002 m
Beach	0	0	0	0	0.25	0.25	0.75	0.5	0.001 m	0.001 m
Sandy Area	0	0	0	0	0.2	0.2	0.2	0.1	0.001 m	0.001 m
Bare Exposed Rock	0	0	0	0	0.15	0.15	0.1	0.05	0.01 m	0.01 m
Quarry_Gravel Pit	0	0	0	0	0.13	0.13	0.2	0.1	0.05 m	0.05 m
Transition Area	0	0	0	0	0.15	0.15	0.2	0.1	0.005 m	0.005 m
Mixed Barren Land	0	0	0	0	0.15	0.15	0.2	0.1	0.005 m	0.005 m
Shrub_Bush Tundra	0	0	0	0	0.7	0.2	0.9	0.5	0.1 m	0.1 m
Herbaceous Tundra	0	0	0	0	0.7	0.2	0.9	0.5	0.02 m	0.02 m
Bare Ground	0	0	0	0	0.25	0.25	0.2	0.1	0.05 m	0.05 m
Wet Tundra	0	0	0	0	0.7	0.15	0.9	0.6	0.05 m	0.05 m
Mixed Tundra	0	0	0	0	0.7	0.15	0.9	0.5	0.05 m	0.05 m
Perennial Snowfield	0	0	0	0	0.6	0.45	0.95	0.95	0.001 m	0.001 m
Glacier	0	0	0	0	0.7	0.55	0.95	0.95	0.01 m	0.01 m

Table 3. Description of land-use categories based on the 30-m resolution of USGS data and physical parameters for winter and summer.

USGS LULC	f_urban	f_roof	h_urban	q_urban	albd_win	albd_sum	gwet_win	gwet_sum	z <sub>0</sub> _win	z <sub>0</sub> _sum
Open Water	0	0	0	0	0.08	0.08	1.0	1.0	0.0001 m	0.0001 m
Perennial Ice / Snow	0	0	0	0	0.65	0.5	0.95	0.95	0.005 m	0.001 m
Low Density Residential	1.0	0.33	10 m	20 W/m**2	0.18	0.18	0.2	0.16	0.2 m	0.2 m
High Density Residential	1.0	0.33	20 m	25 W/m**2	0.18	0.18	0.1	0.06	0.5 m	0.5 m
Commercial_Industrial	1.0	0.33	20 m	25 W/m**2	0.18	0.18	0.1	0.06	0.5 m	0.5 m
Bare Rock_Sand_Clay	0	0	0	0	0.15	0.15	0.1	0.05	0.01 m	0.01 m
Quarry_Gravel Pit	0	0	0	0	0.13	0.13	0.2	0.1	0.05 m	0.05 m
Transitioanal	0	0	0	0	0.15	0.15	0.2	0.1	0.005 m	0.005 m
Deciduous Forest	0	0	0	0	0.17	0.16	0.6	0.3	0.5 m	0.5 m
Evergreen Forest	0	0	0	0	0.12	0.12	0.6	0.3	0.5 m	0.5 m
Mixed Forest	0	0	0	0	0.14	0.14	0.7	0.3	0.5 m	0.5 m
Shrub Land	0	0	0	0	0.23	0.21	0.3	0.15	0.1 m	0.12 m
Orchard_Vineyard	0	0	0	0	0.23	0.18	0.6	0.3	0.07 m	0.2 m
Grassland_Herbaceous	0	0	0	0	0.23	0.19	0.3	0.15	0.1 m	0.12 m
Pasture_Hay	0	0	0	0	0.25	0.21	0.6	0.3	0.06 m	0.18 m
Row Crop	0	0	0	0	0.25	0.21	0.6	0.3	0.06 m	0.18 m
Small Grain	0	0	0	0	0.25	0.21	0.6	0.3	0.01 m	0.02 m
Fallow	0	0	0	0	0.25	0.21	0.6	0.3	0.01 m	0.01 m
Urban_Residential Grass	0	0	0	0	0.1	0.21	0.8	0.3	0.01 m	0.02 m
Woody Wetland	0	0	0	0	0.14	0.14	0.7	0.35	0.4 m	0.4 m
Herbaceous Wetland	0	0	0	0	0.14	0.14	0.75	0.5	0.2 m	0.2 m

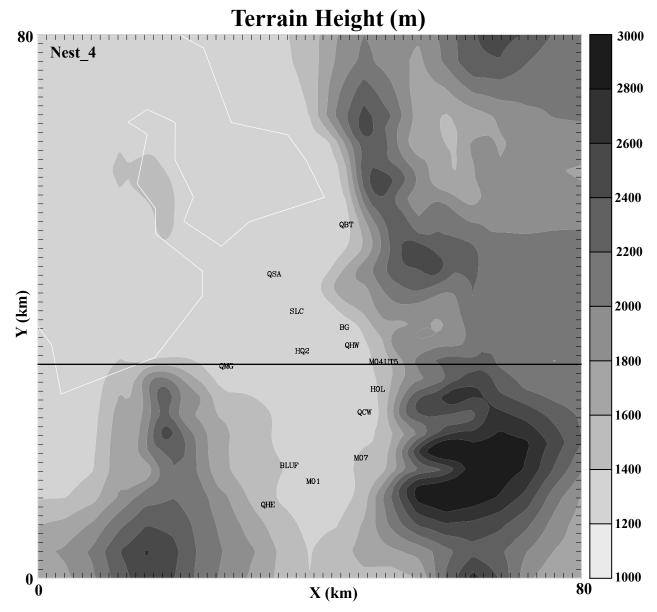


Fig. 1. Terrain height of the nest-4 domain of simulations in unit of meter. The letters mark the locations of surface stations used in this study (see Table 1). The black line across the stations M04 indicates the location of x-z cross-sections shown in this study. To avoid the overlapping of location labels at station BB, BG, and QB, only the station BG is shown in the figure.

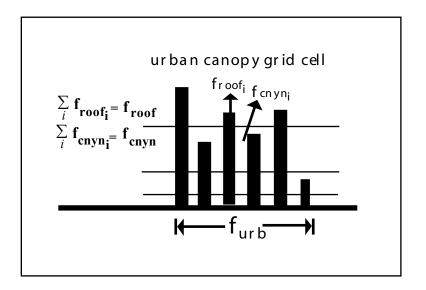


Fig. 2. Two dimensional view of the urban grid configuration in the horizontal and vertical directions. The urban canopy fraction ( $f_{urb}$ ) is further divided into roof fraction ( $f_{roof}$ ) and street canyon fraction ( $f_{cnyn}$ ). The area fraction in the rural region is defined as 1 -  $f_{urb}$ . The actual application is in three dimensions.

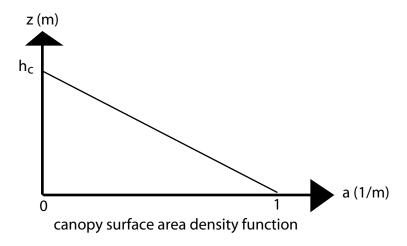


Fig. 3. The building surface area density profile of the urban canopy in this study is assumed to be linearly decreased from the surface to the top of the highest building (i.e., the height of the urban canopy, h<sub>c</sub>).

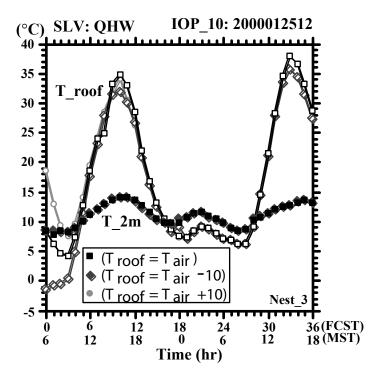


Fig. 4. Time series of the model predicted 2-m air temperature (solid cells) and its corresponding roof temperature (open cells) at the station QHW (see Fig. 1) at every hour of UCP\_30m simulation with the resolution of 4 km. Squared cells are for the run with the initial roof temperature same as air temperature, diamond cells for the simulation with colder initial roof temperatureby 10 °C, and circle cells for the run with warmer initial roof temperature by 10 °C.

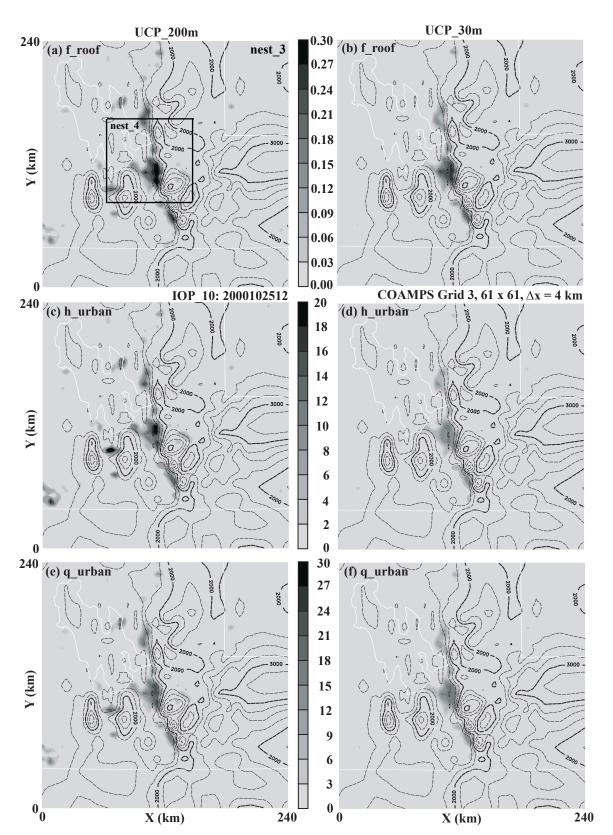


Fig. 5. Horizontal cross-sections of urban infrastructure properties derived from different resolutions of the USGS land-use data over the COAMPS nest-3 domain ( $\Delta x = 4$  km). The left and right panels are for 200-m and 300-m resolutions, respectively. The plots from the top to the bottom are for roof fraction, canopy building height and anthropogenic heating, respectively. The contour lines represent the local terrain heights. The small box in (a) marks the nest-4 domain ( $\Delta x = 1.333$  km).

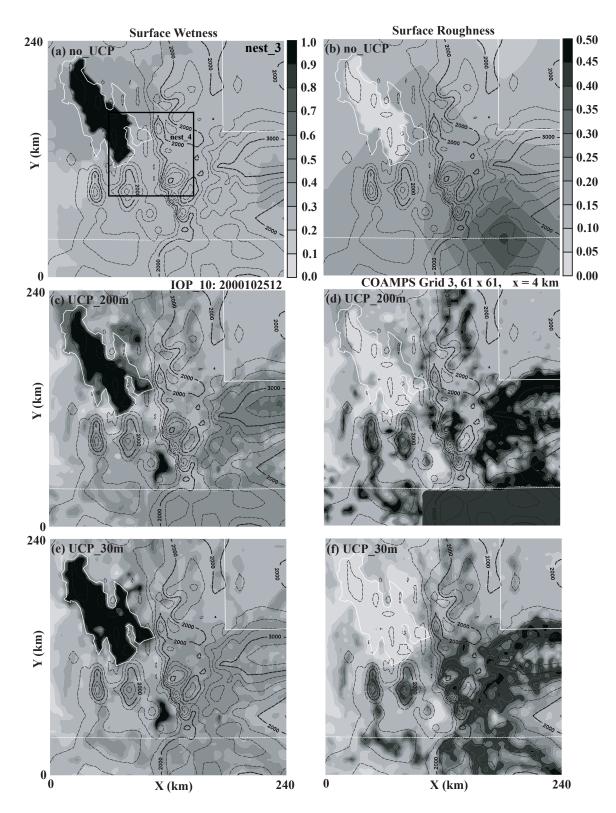


Fig. 6. As in Fig. 5, except for the urban surface properties for ground wetness (left) and roughness (right column), and for varied choices of surface data sources (ETA-40km, UCP\_200m, and UCP\_30m from top to bottom, respectively).

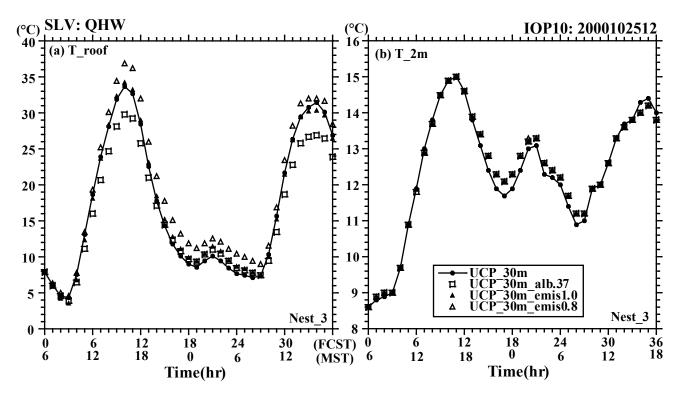


Fig. 7. As in Fig. 4, except for the sensitivity experiments with the rooftop properties having higher albedo (0.37) and varied emissivity (1.0 and 0.8, respectively). (a) for the rooftop temperature at 2 meters above the ground, and (b) 2-m air temperature.

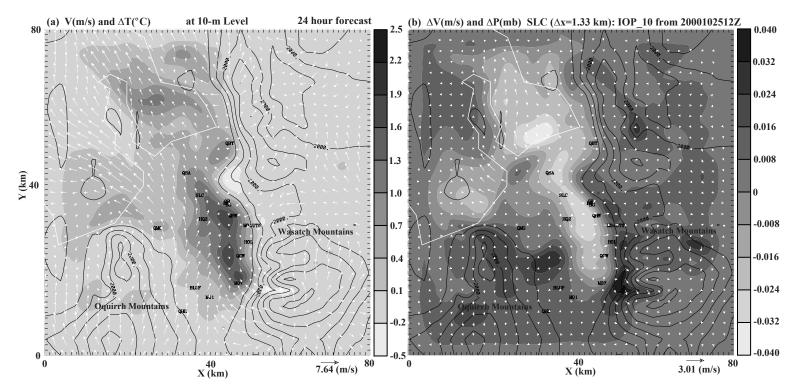


Fig. 8. Horizontal cross-sections of 10-m nighttime forecasts at the 24 hours of the simulation time (i.e., 06h MST, October 26 2000) for the nest-4 of the UCP\_30m run. (a) Horizontal wind vector and temperature deviation, substracted from the one in the no\_UCP run, and (b) the deviations of horizontal wind vector and pressure field defined as (a). Contour lines represent the local terrain heights.

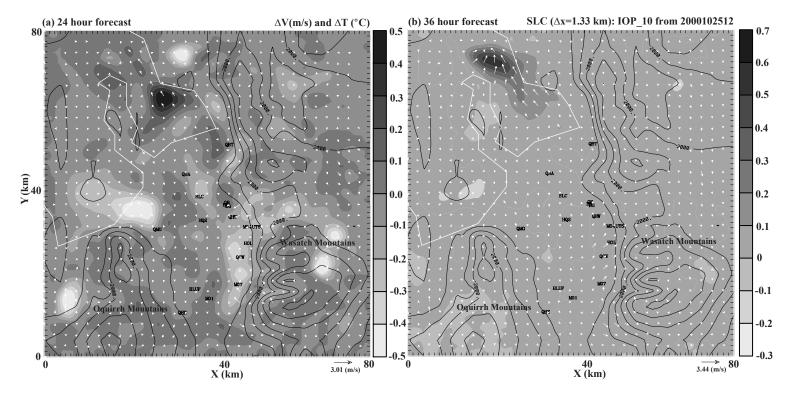


Fig. 9. As in Fig. 8, except for the deviations of 10-m forecasts for horizontal wind and temperature fields. The deviation is defined in the same way as Fig. 8, except for the differences between UCP\_30m and UCP\_200m. (a) 24 hours of forecast (06h MST, October 26 2000), and (b) 36 hours of forecast (18h MST, October 26 2000).

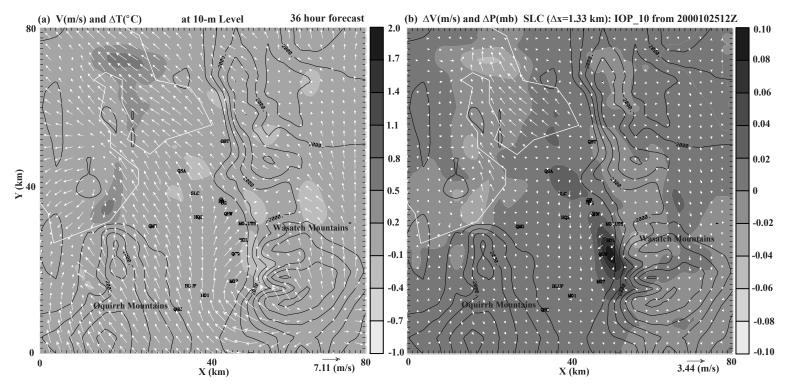


Fig. 10. As in Fig. 8, except for the daytime forecasts of the UCP\_30m run at 36 hours of the simulation time (18h MST, October 26 2000).

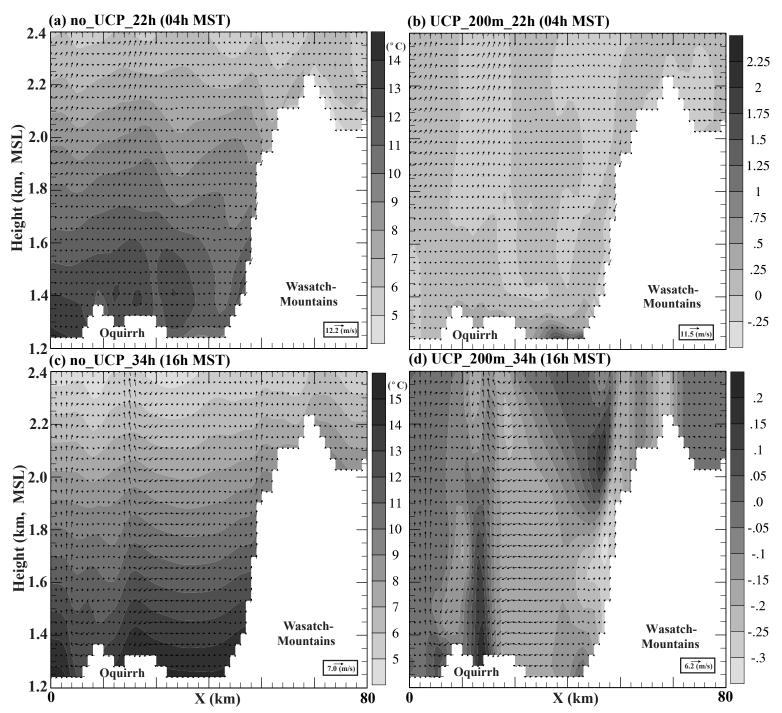


Fig. 11. Vertical cross-sections along the line across the station M04 as shown in Fig. 1. Top and bottom panels are for the nighttime (22 hours of simulation time; 04h MST, October 26 2000) and daytime (34 hours of simulation time; 16h MST, October 26 2000) forecasts, respectively. The wind vectors are plotted for no\_UCP (left) and UCP\_200m (right) simulations in terms of (u, w) components. The vertical wind is enlarged by 10 times to amplify the valley flow. The shading on the left panels is for the temperature forecast of no\_UCP run while the difference of temperature forecast between UCP\_200m and no\_UCP simulations is shown in the right panels.

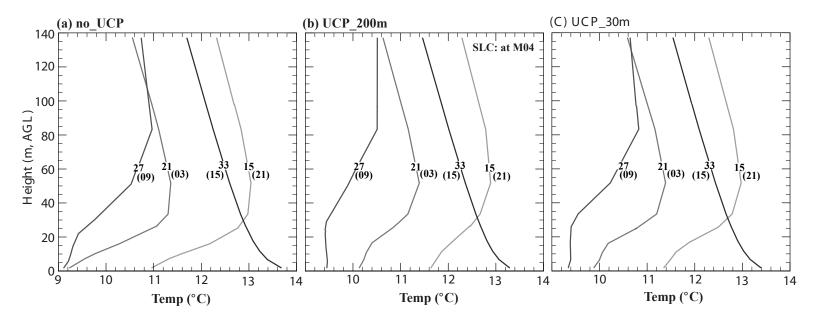


Fig. 12. Evolutions of the vertical profiles for the predicted temperature fields in unit of °C at the model nest-4 grid near the station M04. The curves on the plots are labeled by the forecast time (hour) of the simulation in an interval of 6 hours. The local time (MST) of each labeled forecast time is also shown in the parenthesis. (a) for the no\_UCP run, (b) for the UCP\_200m run, and (c) for the UCP\_30m run.

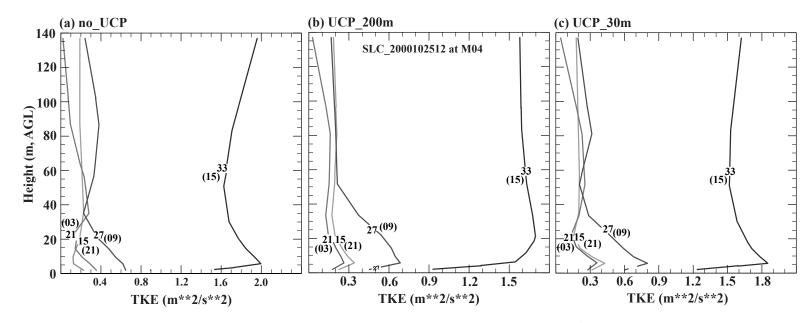


Fig. 13. As in Fig. 12, except for the turbulence kinetic energy field in unit of  $m^2s^{-2}$ .

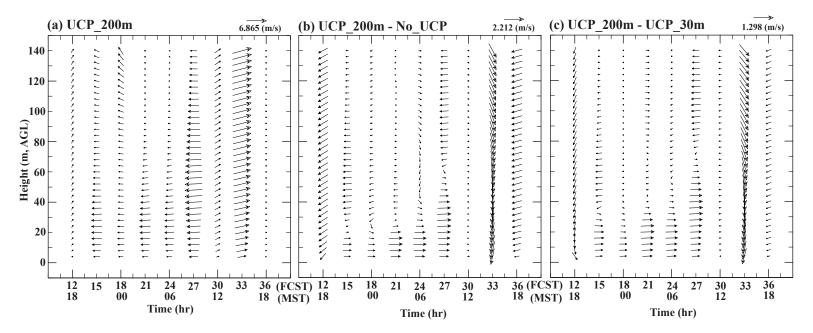


Fig. 14. Evolutions of the vertical profiles for the predicted horizontal winds at the model nest-4 grid near the station M04. (a) for the UCP\_200m run, (b) for the deviation between UCP\_200m and uCP\_30m.

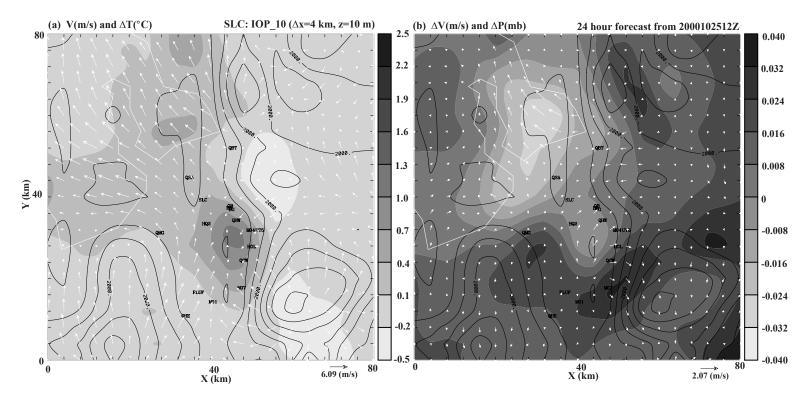


Fig. 15. As in Fig. 8, except for the model nest-3 grid domain.

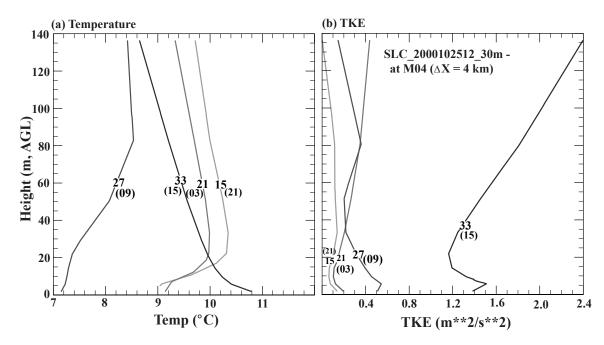


Fig. 16. As in Figs 12a and 13c, except for the nest-3 grid of the UCP\_30m run.

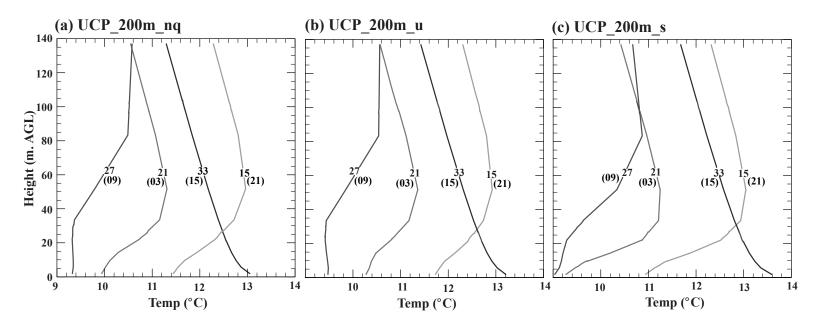


Fig. 17. As in Fig. 12b, except for different urban morphology. (a) no anthropogenic heating, (b) without using land-use data derived urban surface properties, (c) without using land-use data derived urban infrastructure properties.

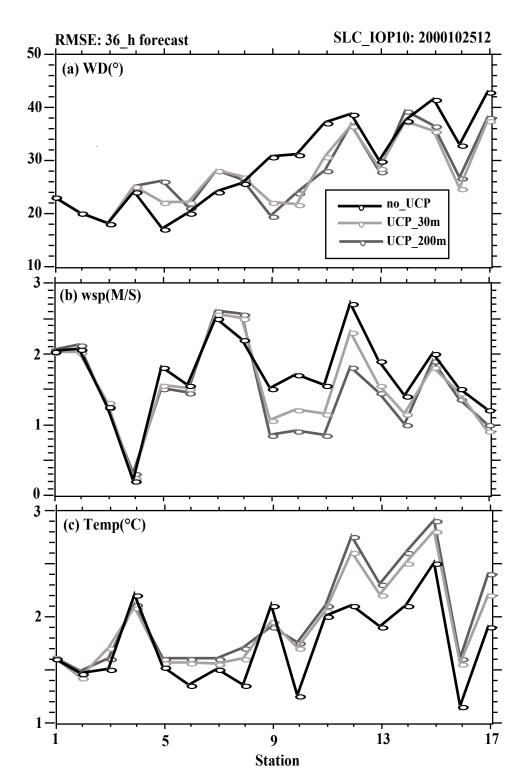


Fig. 18. Root mean square errors (RMSEs) of 36-h forecasts with respect to the surface station measurements for the nest-4 simulations with different configurations of urban properties at selected stations. The stations are labeled in sequence based on the size of roof fraction as shown in Table 1.

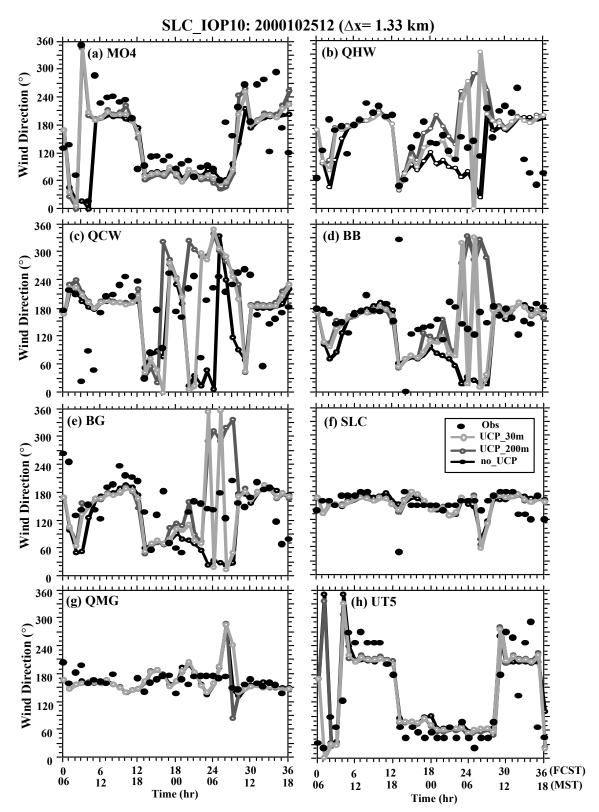


Fig. 19. Evolutions of predicted wind directions throughout 36 hours of the nest-4 simulations at selected surface stations. The instruments of these stations are located at different heights ranging from 2 to 15 meters. The comparison of prediction with observation is made using the value at the closest model grid height. The plots are labeled in sequence based on the size of roof fraction. The locations and the details of these surface stations are shown in Table 1.

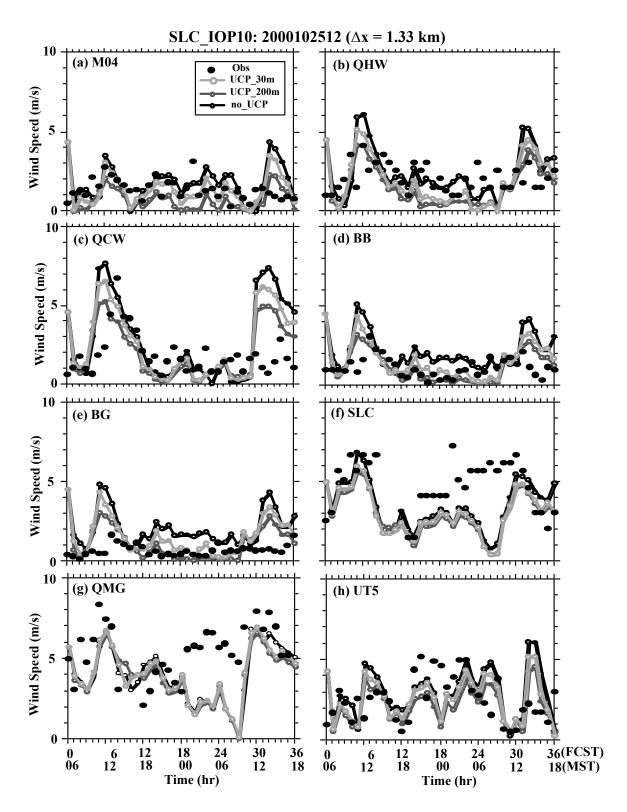


Fig. 20. As in Fig. 19, except for the wind speed comparison.

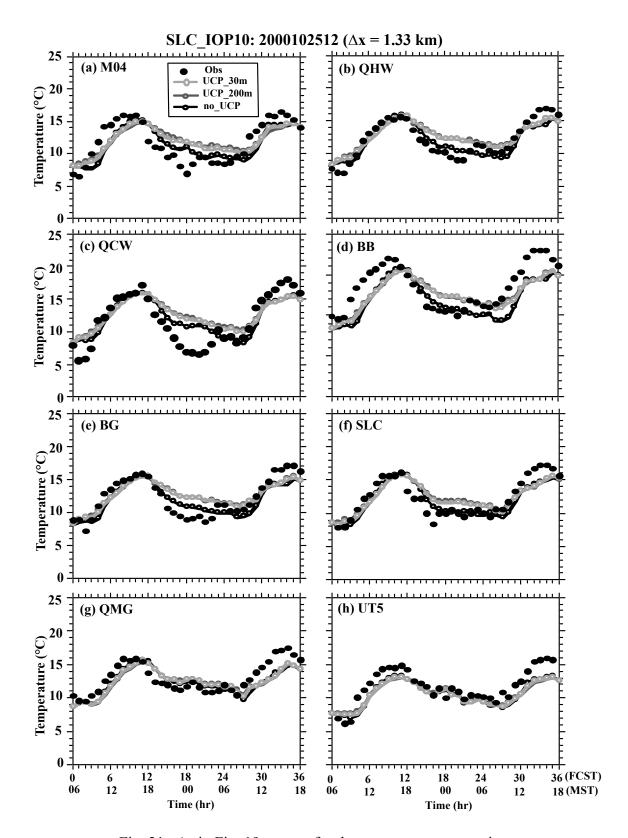


Fig. 21. As in Fig. 19, except for the temperature comparison.

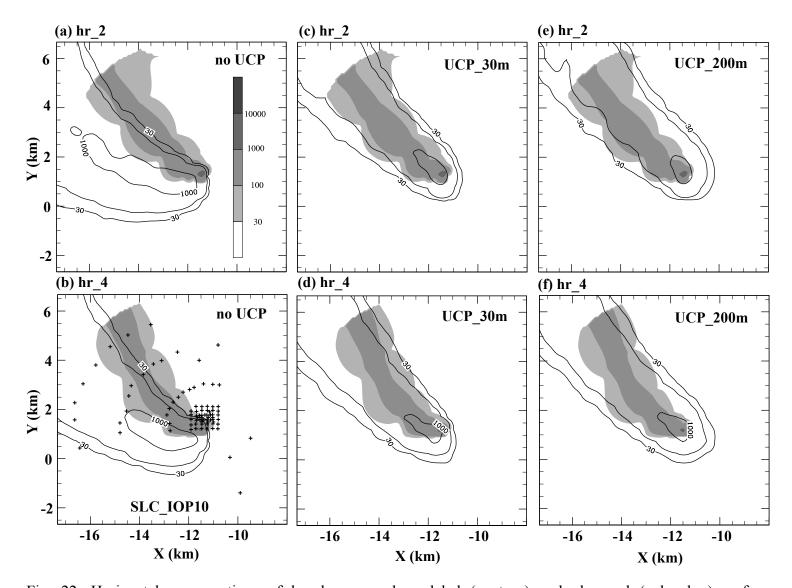


Fig. 22. Horizontal cross-sections of hourly-averaged modeled (contour) and observed (color bar) surface SF<sub>6</sub> concentrations in unitb of parts perb billion. The simulated concentrations are calculated using LLNL's Lagrangian Operational Dispersion Integrator based on COAMPS' prediction without and with the urban canopy parameterization for varied resolutions of land-use data. The parameterization for different resolutions of land-use data. The pictures are shown at the second and fourth hours from the tracer release times, which correspond to 21 and 23 hours of simulation time in the COAMPS forecast. The plus sign shown in (b) marks the locations of NOAA samplers with tracer data.